CAMBRIDGE
UNIVERSITY PRESS

Research Paper

Bridging the ultraviolet and optical regions: Transformation equations between *GALEX* and *UBV* photometric systems

S. Bilir[1] , N. Alan[1], S. Tunçel Güçtekin[1], M. Çelebi[2], T. Yontan[2], O. Plevne[2], S. Ak[1], T. Ak[1] and S. Karaali[1]

[1]Department of Astronomy and Space Sciences, Faculty of Science, Istanbul University, Beyazıt, 34119 Istanbul, Turkey and [2]Institute of Graduate Studies in Science, Programme of Astronomy and Space Sciences, Istanbul University, Beyazıt, 34116 Istanbul, Turkey

Abstract

We derive transformation equations between *GALEX* and *UBV* colours by using the reliable data of 556 stars. We present two sets of equations: as a function of (only) luminosity class and as a function of both luminosity class and metallicity. The metallicities are provided from the literature, while the luminosity classes are determined by using the PARSEC mass tracks in this study. Small colour residuals and high squared correlation coefficients promise accurate derived colours. The application of the transformation equations to 70 stars with reliable data shows that the metallicity plays an important role in estimation of more accurate colours.

Keywords: techniques: photometric – catalogue – surveys

1. Introduction

Reliable spectroscopic, photometric, and astrometric data are important for understanding the structure, formation, and evolution of our Galaxy. Today, sky surveys are systematically carried out in a wide range of the electromagnetic spectrum from X-rays to the radio. In some sky surveys such as *ROSAT* (Snowden 1995), *GALEX* (Martin et al. 2005), and SDSS (York et al. 2000), which are carried out between the X-ray and optical regions of the electromagnetic spectrum, the interstellar absorption prevents to obtain accurate magnitude and colours. However, this problem has been overcame by means of the sky surveys which are defined over the infrared region of the star spectrum, i.e. 2MASS (Skrutskie et al. 2006), UKIDSS (Hewett et al. 1996), VVV (Minniti et al. 2010), VISTA (Cross et al. 2012), *WISE* (Wright et al. 2010), and *AKARI* (Murakami et al. 2007). Thus, considerable information have been obtained, especially on the bulge, bar structure, and Galactic stellar warp in our Galaxy (Dwek et al. 1995; Lopez-Corredoira, Cabrera-Lavers, & Gerhard 2005; Lopez-Corredoira et al. 2019a, b; Benjamin et al. 2005).

Today, photometric sky survey observations are systematically performed to cover the ultraviolet (UV) and infrared regions of the electromagnetic spectrum. In spectroscopic sky surveys, spectroscopic observations are made for a limited number of objects with different luminosities which are classified according to their positions in colour spaces obtained from the photometric observations. The main sequence stars provide information about the solar neighbourhood, and the evolved stars provide information about the old thin disc, thick disc, and halo populations of our Galaxy beyond the solar vicinity. The number of stars observed

on current spectroscopic sky survey programs does not exceed one million in total. As this number is less than needed for a detailed study of the Galactic structure, precise measurements of photometric sky surveys, which contain billions of bright and faint objects, are still important in testing models about the structure and evolution of the Galaxy.

Photometric sky surveys performed in different regions of the electromagnetic spectrum are designed to include shallow or deep magnitudes, according to the purpose of the researchers. However, transformations between different photometric systems can be used as a tool to combine shallow and deep magnitudes. These transformation equations can also be produced in terms of luminosity and metallicity. In the literature, transformation equations are given for main sequence stars (Smith et al. 2002; Karaali, Bilir, & Tunçel 2005; Bilir, Karaali, & Tunçel 2005; Bilir et al. 2008a; Bilir et al. 2011; Rodgers et al. 2006; Jordi et al. 2006; Covey et al. 2007; Chonis & Gaskell 2008) and evolved stars (Straizys & Lazauskaite 2009; Yaz et al. 2010; Bilir et al. 2012, 2013; Ak et al. 2014). Transformation equations between the photometric systems have been obtained for approximately 20 years and used effectively to investigate the structure and evolution of our Galaxy. *UBV* is one of the important photometric system in the optical region (Johnson & Morgan 1953) which is used to determine the photometric metallicities of the stars and the interstellar absorption. The $U - B$ colour index plays an important role in these determinations, while its combination with the colour index $B - V$ can be used in determination of the reddening of stars. In the *UBV* photometric system, the colour excess $E(B - V)$ of a star can be determined by the Q method or by shifting its observed $B - V$ colour index along the reddening vector in the $U - B \times B - V$ two-colour diagram up to the intrinsic colour index $(B - V)_0$ (Johnson & Morgan 1953). While the colour excess $E(U - B)$ can be calculated by the equation of the reddening line, i.e. $E(U - B) = 0.72 \times E(B - V) + 0.05 \times E(B - V)^2$. Roman (1955) discovered that stars with weak metal lines have

Table 1. Spectroscopic data used in this study. N denotes the number of stars, R spectral resolution, S/N signal-to-noise ratio. Observatory, telescope, and the spectrograph used in the observations are also noted.

ID	Authors	N	R	*S/N*	Observatory/Telescope/Spectrograph
1	Boesgaard et al. (2011)	117	∼ 42 000	106	Keck/Keck I/HIRES
2	Nissen & Schuster (2011)	100	55 000	250–500	ESO/VLT/UVES, ORM/NOT/FIES
3	Ishigaki et al. (2012)	97	100 000	140–390	NAOJ/Subaru/HDS
4	Mishenina et al. (2013)	276	42 000	> 100	Haute-Provence/1.93m/ELODIE
5	Molenda-Zakowicz et al. (2013)	221	25 000–46 000	80–6500	ORM/NOT/FIES, OACt/91cm/FRESCO, ORM/Mercator/HERMES
					OPM/TBL/NARVAL, MKO/CFHT/ESPaDOnS
6	Bensby et al. (2014)	714	40 000–110 000	150–300	ESO/1.5m and 2.2m/FEROS, ORM/NOT/SOFIN and FIES,
					ESO/VLT/UVES, ESO/3.6m/HARPS, Magellan Clay/MIKE
7	da Silva et al. (2015)	309	∼ 42 000	> 150	Haute Provence/1.93m/ELODIE
8	Sitnova et al. (2015)	51	> 60 000	70–100	Lick/Shane 3m/Hamilton, CFH/CFHT/ESPaDOnS
9	Jofré et al. (2015)	223	30 000–120 000	> 150	ESO/3.6m/HARPS, ESO/2.2 m/FEROS, OHP/1.93m/ELODIE,
					OHP/1.93m/SOPHIE, CASLEO, 2.15m/EBASIM
10	Brewer et al. (2016)	1 615	∼ 70 000	> 200	Keck/Keck I/HIRES
11	Kim et al. (2016)	170	10 000	> 100	KPNO/Mayall 4m/Echelle spectrograph
12	Maldonado & Villaver (2016)	154	∼ 42 000–115 000	107	La Palma/Mercator/HERMES, ORM/NOT/FIES,
					Calar Alto/2.2m/FOCES, ORM/Nazionale Galileo/SARG
13	Luck (2017)	1 041	30 000–42 000	> 75	McDonald/2.1m/SCES, McDonald/HET/High-Resolution
14	Delgado Mena et al. (2017)	1 059	∼ 115 000	> 200	HARPS GTO programs

CASLEO: Complejo Astronomico El Leoncito, EBASIM: Echellede Banco Simmons, CFH: Canada-France-Hawaii, CFHT: Canada-France-Hawaii Telescope, ESO: European Southern Observatory, ESPaDOnS: an Echelle SpectroPolarimetric Device for the Observation of Stars at CFHT, FEROS: The Fiber-Fed Extended Range Optical Spectrograph, FIES: The High-Resolution Fibre-Fed Echelle Spectrograph, FOCES: a Fibre Optics Cassegrain Echelle Spectrograph, FRESCO: Fiber-Optic Reosc Echelle Spectrograph of Catania Observatory, GTO: Guaranteed Time Observations, HARPS: High Accuracy Radial Velocity Planet Searcher, HERMES: High-Efficiency and High-Resolution Mercator Echelle Spectrograph, HET: Hobby-Eberly Telescope, HDS: High Dispersion Spectrograph, HIRES: High-Resolution Echelle Spectrometer, KPNO: Kitt Peak National Observatory, MIKE: Magellan Inamori Kyocera Echelle, MKO: Mauna Kea Observatory, NAOJ: National Astronomical Observatory of Japan, NOT: Nordic Optical Telescope, OACt: Catania Astrophysical Observatory, OPM: Observatorie Pic du Midi, ORM: Observatorio del Roque de losMuchachos, SCES: Sandiford Cassegrain Echelle Spectrograph, SOFIN: The Soviet-Finnish Optical High-Resolution Spectrograph, SOPHIE: Spectrographe pour l'Observation des Phenomenes des Interieurs stellaires et des Exoplanetes, TBL: Telescope Bernard Lyot, UVES: Ultraviolet and Visual Echelle Spectrograph, VLT: Very Large Telescope.
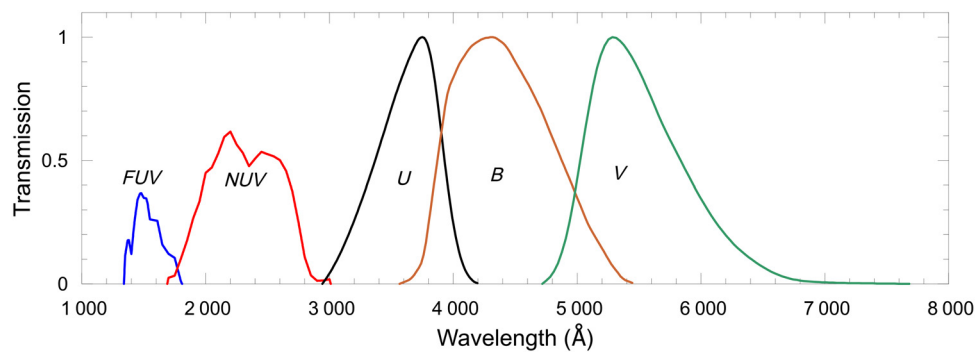

Figure 1. Normalized transmission curves of the *GALEX FUV*, *NUV* and Johnson-Morgan *U*, *B*, *V* filters.

larger ultraviolet (UV) excesses than the ones with strong metal lines. Schwarzschild, Searle, & Howard (1955), Sandage & Eggen (1959), and Wallerstein (1962) confirmed the work of Roman (1955). Thus, metal-rich and metal-poor stars could be classified not only spectroscopically but also photometrically, i.e. by their UV excesses. Sandage (1969) noticed in a $(U - B)_0 \times (B - V)_0$ two-colour diagram of a set of stars in solar neighbourhood that stars with the same metallicity have a maximum UV excess at the colour index $(B - V)_0 = 0.6$ mag and introduced a procedure to reduce the UV excesses of the stars to the one of colour

index $(B - V)_0 = 0.6$ mag. The relation between the UV excess and metallicities of stars has been used by the researchers for their metallicity estimation via photometry (i.e. Carney 1979; Karaali et al. 2003a, b, c; Karataş & Schuster 2006; Karaali et al. 2011; Tunçel Güçtekin et al. 2016; Çelebi et al. 2019). Similar calibrations have been developed for the SDSS photometric system and applied to faint stars (Karaali et al. 2005; Bilir et al. 2005; Tunçel Güçtekin et al. 2017). These calibrations were used to calculate metal abundances (Ak et al. 2007; Ivezic et al. 2008; Tunçel Güçtekin et al. 2019) and estimation of the Galactic model parameters

Table 2. The basic parameters of 556 sample stars; ID, star, equatorial coordinates in J2000 (α, δ), photometric data (*FUV*, *NUV*, *V*, *U* − *B*, *B* − *V*), reduced colour excess ($E_d(B - V)$), atmospheric model parameters (T_{eff}, log g and [Fe/H]) and their references, and trigonometric parallaxes (π) with the errors taken from *Gaia* DR2.

ID	Star	α (hh:mm:ss)	δ (dd:mm:ss)	FUV (mag)	NUV (mag)	V (mag)	U − B (mag)	B − V (mag)	$E_d(B-V)$ (mag)	T_{eff} (K)	log g (cm s^{-2})	[Fe/H] (dex)	Reference	π (mas)	σ_π (mas)
1	Hip 80	00 00 58.28	−11 49 25.50	20.026	13.123	8.400	−0.080	0.550	0.012	5 856	4.10	−0.59	(6)	13.9286	0.0691
2	HD 225197	00 04 19.79	−16 31 44.50	21.159	14.675	5.780	1.054	1.080	0.012	4 778	2.66	0.11	(7)	9.8054	0.0946
3	HD 249	00 07 22.56	+26 27 02.20	22.101	15.353	7.381	0.750	0.995	0.015	4 775	2.95	−0.04	(10)	7.6866	0.0371
4	HD 870	00 12 50.25	−57 54 45.40	19.946	13.660	7.226	0.344	0.774	0.001	5 381	4.42	−0.10	(14)	48.4741	0.0263
5	Hip 1128	00 14 04.48	−11 18 41.70	21.027	13.565	8.360	0.015	0.655	0.009	5 522	4.37	−0.64	(6)	23.3418	0.0534
. . .	. . .	. . .	. . .	. . .	. . .	. . .	. . .	. . .	. . .	. . .	. . .	. . .	. . .	. . .	. . .
. . .	. . .	. . .	. . .	. . .	. . .	. . .	. . .	. . .	. . .	. . .	. . .	. . .	. . .	. . .	. . .
. . .	. . .	. . .	. . .	. . .	. . .	. . .	. . .	. . .	. . .	. . .	. . .	. . .	. . .	. . .	. . .
552	Hip 117526	23 50 05.74	+02 52 37.82	21.482	14.599	8.339	0.362	0.744	0.010	5 540	4.35	0.20	(6)	21.3273	0.0588
553	HD 223524	23 50 14.73	−09 58 26.90	21.009	14.832	5.941	1.150	1.130	0.015	4 656	2.58	0.10	(13)	10.4176	0.0925
554	Hip 117946	23 55 26.60	+22 11 35.80	20.229	16.266	8.770	0.810	1.020	0.006	4 790	4.52	0.04	(10)	39.1780	0.0580
555	Hip 118115	23 57 33.52	−09 38 51.10	20.277	13.434	7.863	0.146	0.641	0.011	5 833	4.39	0.02	(6)	19.4670	0.0642
556	Hip 118278	23 59 28.43	−20 02 05.00	20.803	14.054	7.470	0.290	0.740	0.004	5 533	4.41	−0.07	(11)	38.1312	0.0519
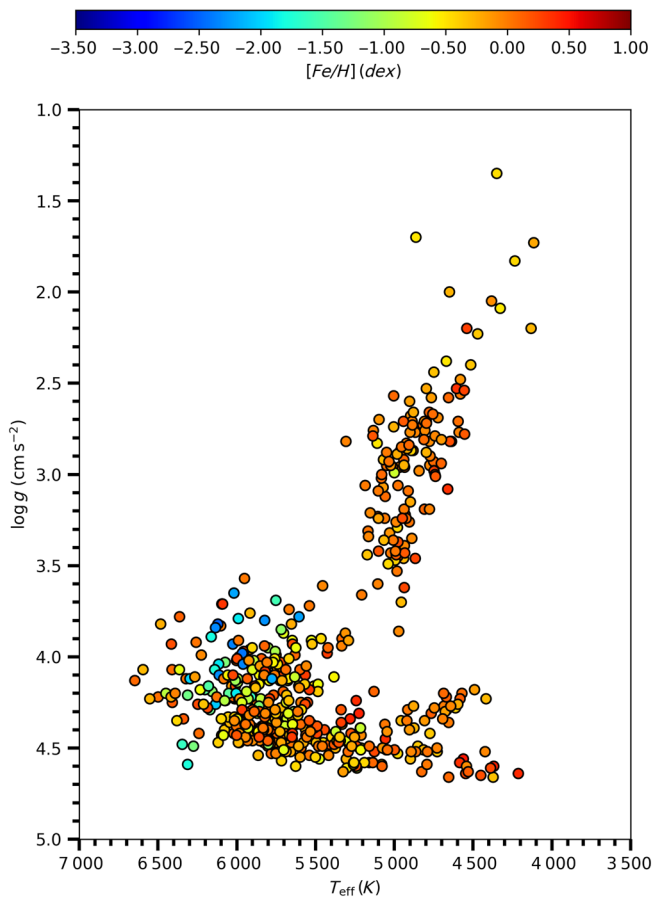
Figure 2. log g × T_{eff} diagram of the stars in the sample. The diagram is colour-coded for the metallicity of 556 stars.

for different populations (Karaali, Bilir, & Hamzaoğlu 2004; Ak et al. 2007; Bilir et al. 2008b; Juric et al. 2008; Yaz & Karaali 2010).

The *UBV* photometric system provides reliable data for the bright stars which occupy the solar neighbourhood. However, for the faint stars the same case thus not hold. Additionally, the low transmission of the Earth's atmosphere limits the number of stars with reliable *U* magnitudes. This problem could be solved by measurements performed outside of the atmosphere such as the satellite Galaxy Evolution Discovery (*GALEX*) (Martin et al. 2005).

The *GALEX* satellite was launched in 2003 and continued its active mission until 2012. It is the first satellite to observe the entire sky with the two detectors, i.e. far ultraviolet (*FUV*, $\lambda_{eff} = 1\,528$ Å; 1 344–1 786 Å) and near ultraviolet (*NUV*, $\lambda_{eff} = 2\,310$ Å; 1 771–2 831 Å). The passbands of *GALEX* and *UBV* photometric systems are shown in Figure 1. Measurements in the far and near UV bands of approximately 583 million objects obtained from the reduction of 100 865 images from satellite observations are given in DR 6+7 versions of *GALEX* database (Bianchi, Shiao, & Thilker 2017). In our study, transformation equations between the colour indices of *GALEX* and *UBV* photometric systems are derived in terms of the luminosity class. These equations provide us empirical *U* − *V* colour index and UV excess for stars which can be used in photometric metal abundance estimation. We organized the paper as follows. Section 2 is devoted to the selection of the calibration stars in our study, derivation of the calibrations is given in Section 3, and finally, the results and discussion are presented in Section 4.

2. Data

In this study, we prioritized the stars that have precise spectroscopic, astrometric, and photometric data in the literature. In this context, we used the spectroscopic data from 14 studies (Boesgaard et al. 2011; Nissen & Schuster 2011; Ishigaki, Chiba, & Aoki 2012; Mishenina et al. 2013; Molenda-Zakowicz et al. 2013; Bensby, Feltzing, & Oey 2014; da Silva, Milone, & Rocha-Pinto, 2015; Sitnova et al. 2015; Jofré et al. 2015; Brewer et al. 2016; Kim et al. 2016; Maldonado & Villaver 2016; Luck 2017; Delgado Mena et al. 2017). Totally, 6 149 stars with atmospheric model parameters (T_{eff}, log g and [Fe/H]) could be provided from
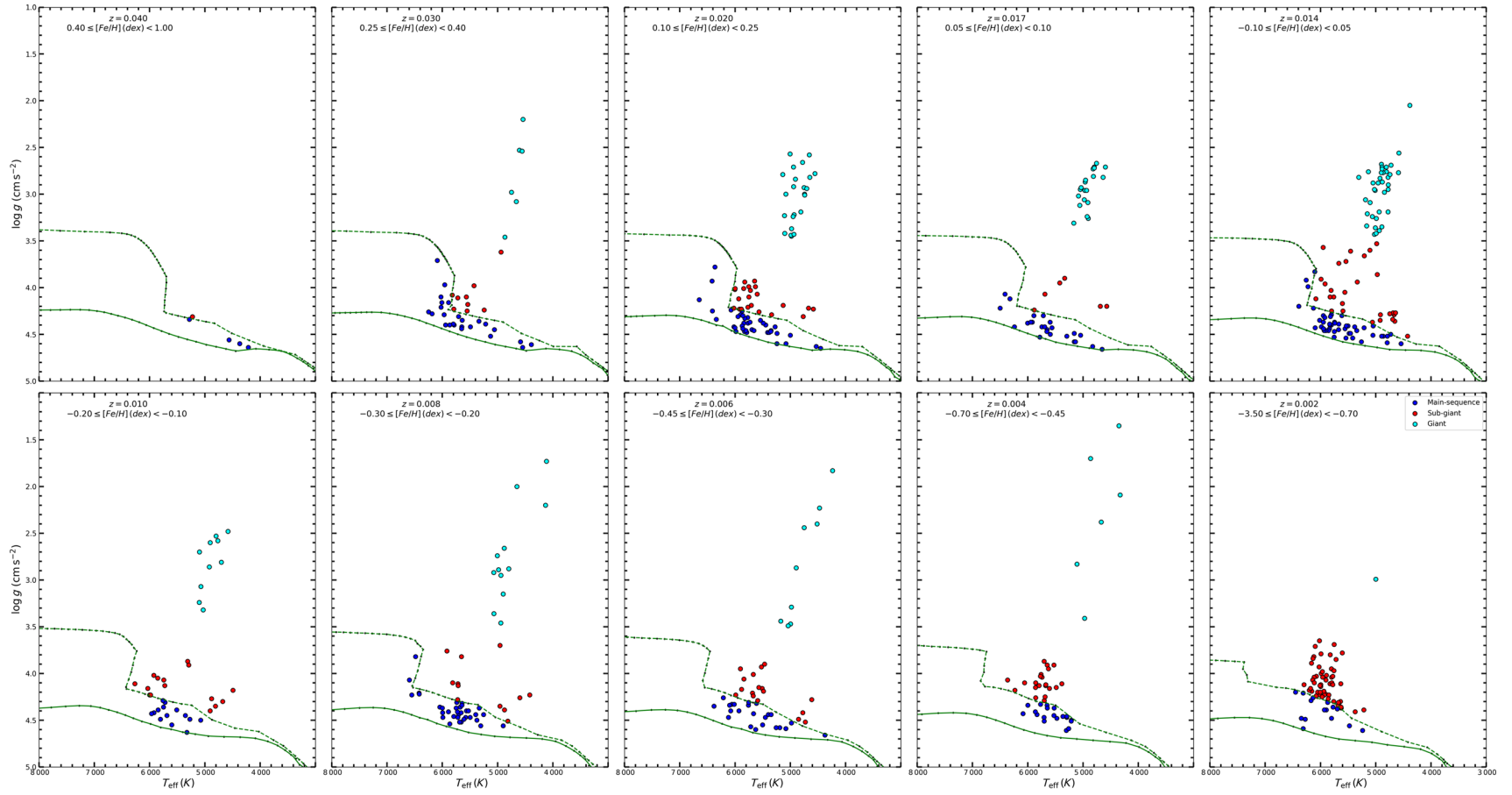
Figure 3. $\log g \times T_{eff}$ diagram of the stars with different metallicity intervals. Blue circle: main sequence, red circle: sub-giants and cyan circle: giant stars. Green solid and dashed curves represent the ZAMS and TAMS, respectively.

Table 3. Distribution of 556 sample stars according to the luminosity classes and the metallicity intervals.

	[Fe/H] ≤ −1	−1 < [Fe/H] ≤ −0.5	−0.5 < [Fe/H] ≤ +0.5	Total
	(dex)	(dex)	(dex)	
Main sequence	7	26	212	245
Sub-giant	38	35	114	187
Giant	–	5	119	124

these studies (Table 1). The photometric data are supplied from *GALEX* DR7 (Bianchi et al. 2017) and *UBV* (Oja 1984; Mermilliod 1987, 1997; Ducati 2002; Koen et al. 2010; Carrasco et al. 2010), while the trigonometric parallaxes are taken from *Gaia* DR2 (Gaia Collaboration et al. 2018). The photometric and astrometric data of 5 593 stars were not available for the original set of stars (6 149 stars). Hence, our sample reduced to 556 (Table 2).

The $\log g \times T_{eff}$ diagram of the sample stars is shown in Figure 2 with the colour coded for metallicity [Fe/H]. PARSEC mass tracks for different metal abundances are used to determine the luminosity classes of the sample stars (Bressan et al. 2012; Tang et al. 2014; Chen et al. 2015). The evolutionary tracks generated for different heavy element abundances ($Z = 0.040, 0.030, 0.020, 0.017, 0.014, 0.010, 0.008, 0.006, 0.004$, and 0.002) are converted to [Fe/H] metallicities using the formulae given by Jo Bovy[a] (see also Bostanci et al. 2018; Eker et al. 2018; Yontan et al. 2019; Banks et al. 2020). Then, zero age main sequence (ZAMS) and terminal age main sequence (TAMS) evolutionary tracks corresponding to the metal abundance ranges for mean Z values were established (Figure 3). The luminosity classes of the sample stars were determined by the metallicity intervals as indicated in Figure 3 and marked on the $\log g \times T_{eff}$ diagrams. Stars between the ZAMS and TAMS curves are classified as main sequence stars, while the ones above the TAMS curve are adopted as evolved stars, i.e. those with $\log g \geq 3.5$ as sub-giants and the ones with $\log g < 3.5$ as giants. Thus, the number of stars with different luminosity classes turned out to be as follows: 245 main sequence, 187 sub-giants, and 124 giants.

We used the atmospheric model parameters to classify the luminosity class of each star. The giant stars tend to be well separated from the sub-giants, while the sub-giants are very close to the main sequence stars. Hence, we investigated the uncertainty of the atmospheric model parameters to reveal any contamination of the sub-giants into the main sequence region and vice versa, as explained in the following. As the uncertainty of the atmospheric model parameters was not considered in some studies which cover our sample stars (556 stars), we used the uncertainty of the atmospheric model parameters in Bensby et al. (2014) which contains approximately 22% of the stars in the sample, for our purpose. The median errors of T_{eff}, $\log g$, and [Fe/H] in Bensby et al. (2014) are 56 K, 0.08 cm s^{-2}, and 0.05 dex, respectively. The luminosity classes of the stars in the sample were determined by comparing the atmospheric model parameters of the stars with the ZAMS and TAMS curves designated from the PARSEC mass tracks. The median errors of the atmospheric model parameters were added to the original parameters of the stars, and their luminosity classes were reassigned. Stars, whose luminosity classes
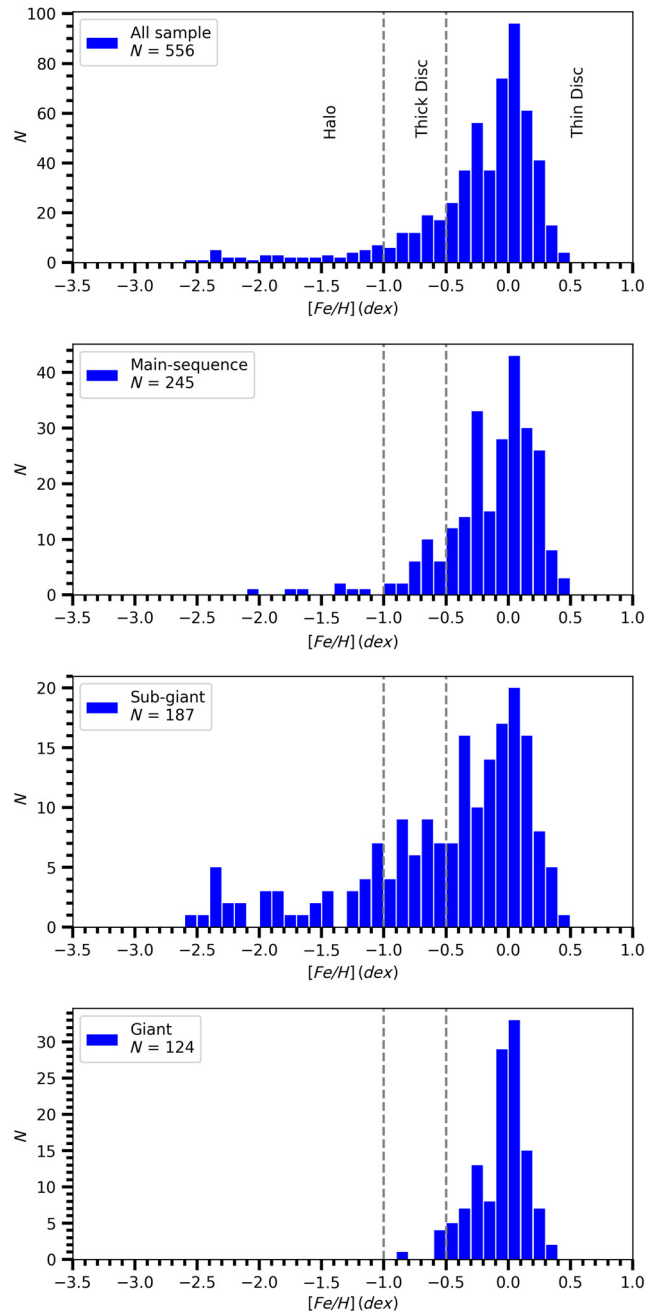
Figure 4. Distribution of the spectroscopic metal abundances for all sample, main sequence, sub-giant, and giant stars.

were changed, were considered as contamination. It is found that the contamination of the main sequence stars by sub-giant stars is 2.9%, the contamination of sub-giant stars by main sequence is 3.7%, and the contamination of giant stars by sub-giant stars is 3.2%. Hence, one can say that our transformation equations can be considered for the luminosity class of the sample stars in question.

The sample stars were also separated into different population types according to their metallicities, i.e. thin disc ($-0.5 < $ [Fe/H] $< +0.5$ dex), thick disc ($-1 < $ [Fe/H] < -0.5 dex), and halo ([Fe/H] < -1 dex), and they were listed in Table 3. The
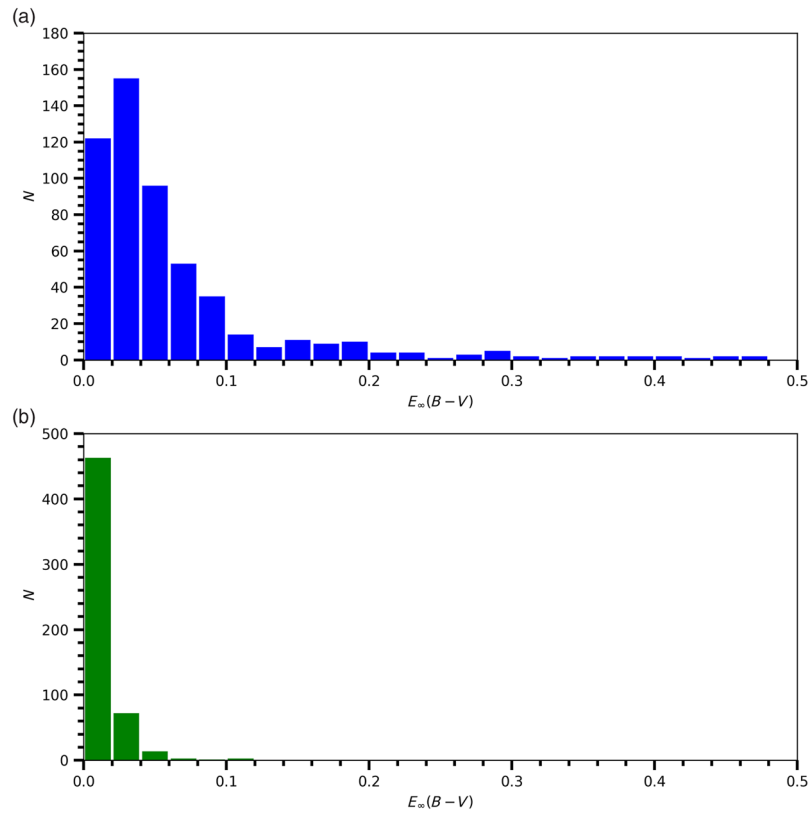
Figure 5. Histograms of the original $E_\infty(B - V)$ (a) and reduced $E_d(B - V)$ (b) colour excesses of 556 stars.
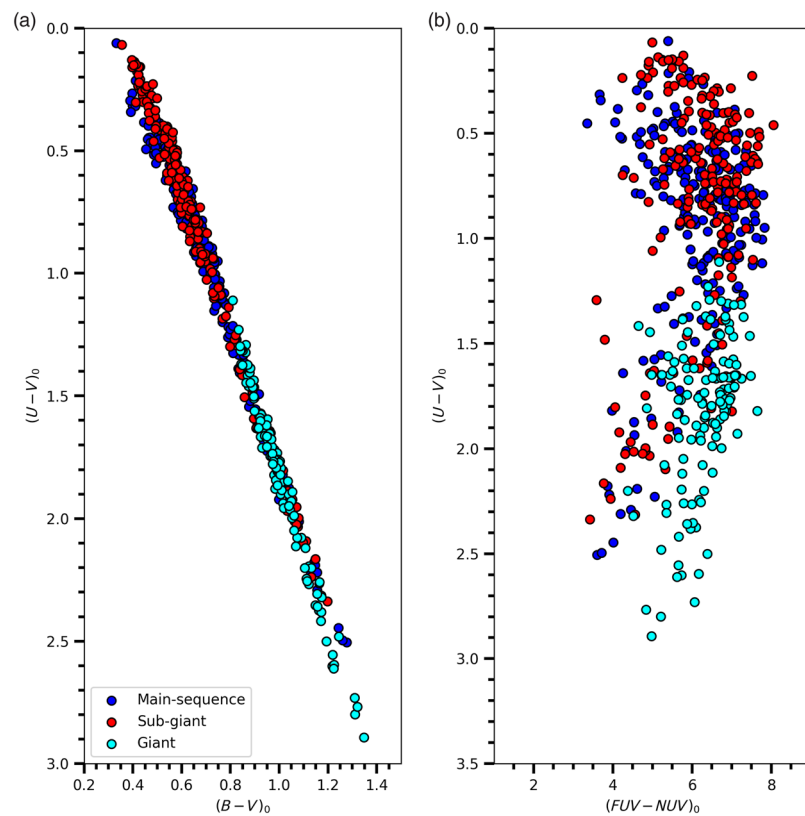
Figure 6. Distribution of the sample stars in the $(U - V)_0 \times (B - V)_0$ (a) and $(U - V)_0 \times (FUV - NUV)_0$ (b) two-colour diagrams, colour coded for the luminosity class as indicated.

Table 4. Coefficients derived from Equation (4) and the corresponding squared correlation coefficient (R^2) and standard deviation (σ), for the sample stars of different luminosity classes. The metallicities are not considered in these calculations. N indicates the number of stars. The remaining symbols are explained in the text.

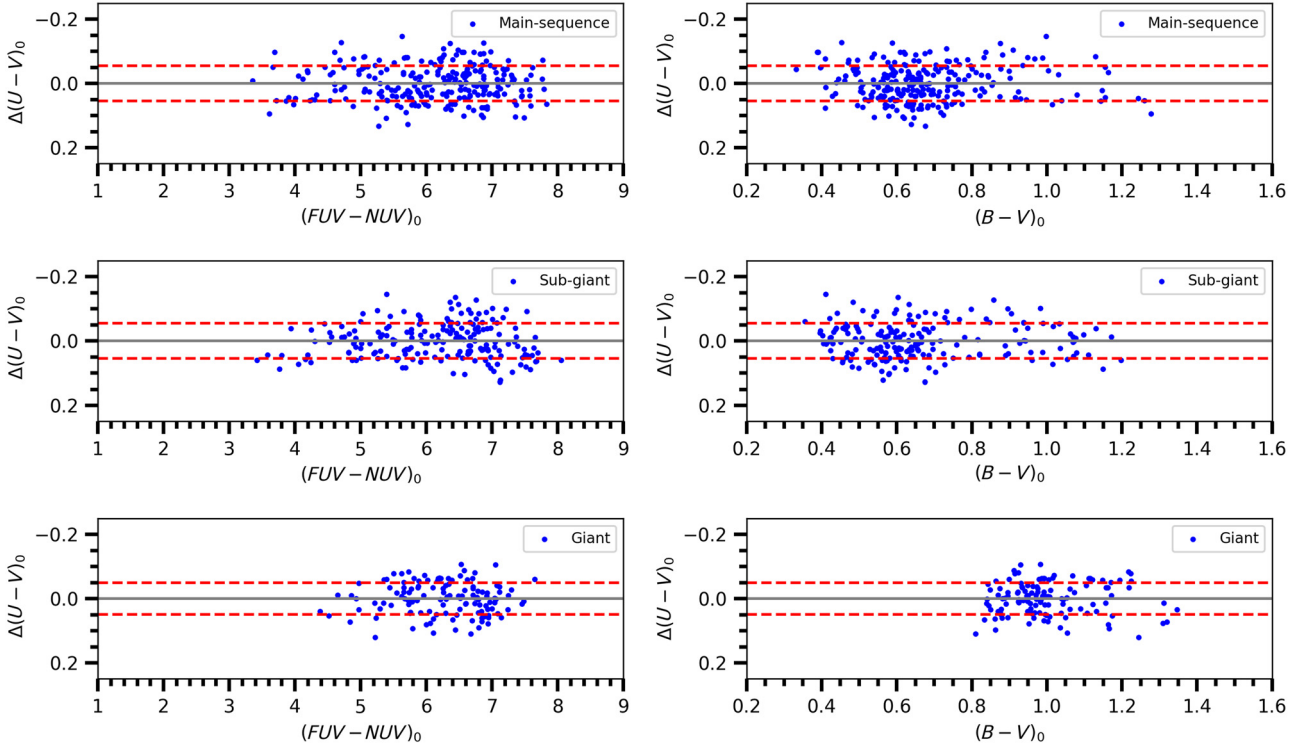| Luminosity class	N	a	b	c	R^2	σ
		$-0.042159(0.003659)$	$2.65427(0.02125)$	$-0.63791(0.02827)$		
Main sequence	245	$T = -11.52$	$T = 124.90$	$T = -22.57$	0.985	0.055
		$p = 0.000$	$p = 0.000$	$p = 0.000$		
		$-0.020667(0.004340)$	$2.79537(0.02161)$	$-0.88118(0.03417)$		
Sub-giant	187	$T = -4.76$	$T = 129.35$	$T = -25.79$	0.990	0.055
		$p = 0.000$	$p = 0.000$	$p = 0.000$		
		$0.002630(0.007415)$	$3.18474(0.04374)$	$-1.37664(0.07691)$		
Giant	124	$T = 0.35$	$T = 72.82$	$T = -17.90$	0.982	0.050
		$p = 0.723$	$p = 0.000$	$p = 0.000$		
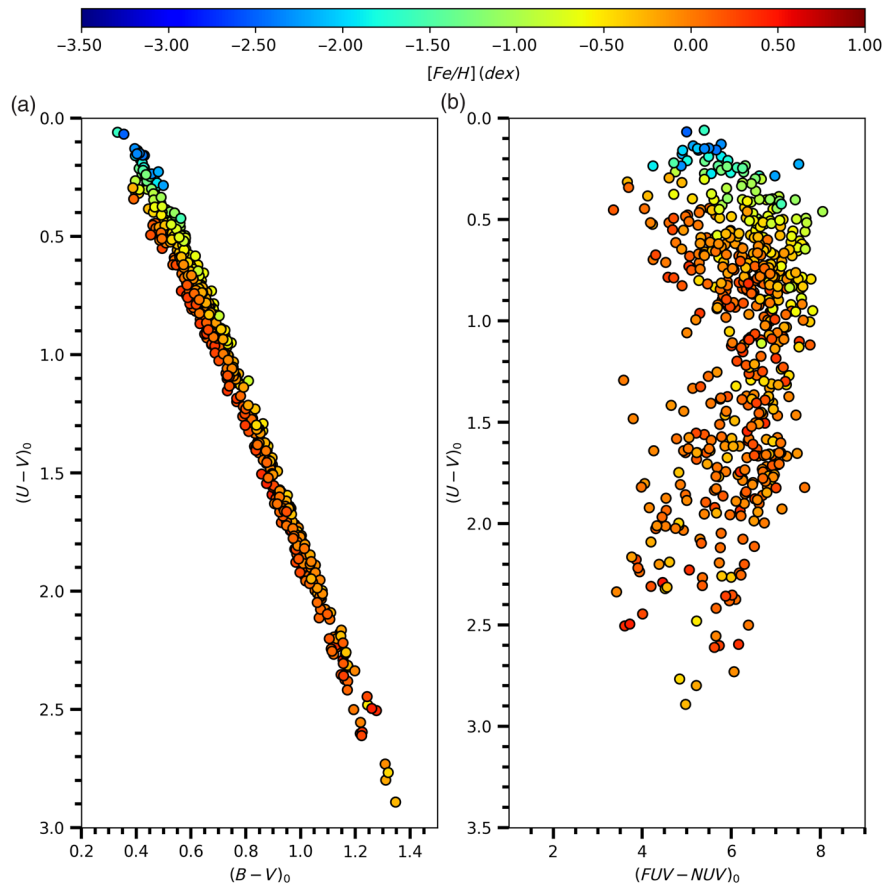
Figure 7. Distribution of the sample stars in the $(U - V)_0 \times (B - V)_0$ (a) and $(U - V)_0 \times (FUV - NUV)_0$ (b) two-colour diagrams, colour coded for the metallicity as indicated.

metallicity distribution for all stars and for different luminosity classes is given in Figure 4.

We estimated the interstellar absorption in the UBV system for the sample stars by using the dust map of Schlafly & Finkbeiner (2011) and reduced it to the distance of the star in question by the following equation of Bahcall & Soneira (1980):

$$A_d(b) = A_\infty(b)\left[1 - \exp\left(\frac{-\mid d \sin(b) \mid}{H}\right)\right]. \quad (1)$$

Here, d and b are the distance and Galactic latitude of a star, respectively, and H indicates the scale height of the Galactic dust ($H = 125$ pc; Marshall et al. 2006). Distances of the stars are

Figure 8. Colour residuals in terms of $(FUV - NUV)_0$ (left column) and $(B - V)_0$ (right column) for three luminosity classes as indicated in six panels. Metallicity is not considered in calculation of the residuals. Dashed lines denote $\pm 1\sigma$ prediction levels.

calculated by using the trigonometric parallaxes in *Gaia* DR2 via the equation $d(\text{pc}) = 1000\,\pi^{-1}(\text{mas})$. The median distances of the main sequence, sub-giant, and giant stars are 33, 49, and 83 pc, respectively. Thus, the colour excesses $E_d(B - V)$ and $E_d(U - B)$ could be calculated by replacing the total absorption $A_d(b)$ in the following equations of Cardelli, Clayton, & Mathis (1989) and Garcia, Claria, & Levato (1988):

$$E_d(B - V) = A_d(b)/3.1 \tag{2}$$

$$E_d(U - B) = 0.72 \times E_d(B - V) + 0.05 \times E_d(B - V)^2$$

Then, we estimated the intrinsic colours and magnitudes by using the following equations. Extinction coefficients in the equations are taken from Cardelli et al. (1989) and Yuan, Liu, & Xiang (2013):

$$(B - V)_0 = (B - V) - E_d(B - V) \tag{3}$$

$$(U - B)_0 = (U - B) - E_d(U - B)$$

$$V_0 = V - 3.1 \times E_d(B - V)$$

$$(FUV)_0 = FUV - 4.37 \times E_d(B - V)$$

$$(NUV)_0 = NUV - 7.06 \times E_d(B - V)$$

Distribution of the colour excesses $E_\infty(B - V)$ and $E_d(B - V)$ are plotted in Figure 5. Small colour excesses indicate that our star sample consists of solar neighbourhood stars. The two-colour diagrams, $(U - V)_0 \times (B - V)_0$ and $(U - V)_0 \times (FUV - NUV)_0$, of the sample stars are plotted in Figures 6 and 7 with colour coded for the luminosity class and metallicity, respectively.

3. Transformation equations

We derived transformation equations between the $(FUV - NUV)_0$ and $(U - V)_0$ colour indices as a function of luminosity class as well as metallicity.

3.1. Transformation equations according to luminosity classes of stars

We adopted the following equation to transform the $(FUV - NUV)_0$ colour index to the $(U - V)_0$ as a function of the luminosity class,

$$(U - V)_0 = a(FUV - NUV)_0 + b(B - V)_0 + c \tag{4}$$

The numerical values of the coefficients a, b, and c estimated for 245 main sequence stars, 187 sub-giants, and 124 giants by using multiple regression method are given in Table 4. T and p values corresponding to the sensitivity of the coefficients are given in the third and fourth lines for each coefficient, while the squared correlation coefficients and the standard deviations are given in the last two columns of the table. One can see that the correlation coefficients are rather high, while the standard deviations are small. The residuals for the colour index $(U - V)_0$, the differences between the original colour indices and the estimated ones are rather small, and no systematic differences can be seen in their distribution (Figure 8). However, there is an exception for the giants, i.e. the uncertainty for the coefficient a is larger than itself, additionally the corresponding p value is greater than the usual one, $p = 0.05$.

Table 5. Coefficients derived from Equation (4) and the corresponding statistical results for sample stars of different luminosity classes and metallicities. *N* indicates the number of stars. The remaining symbols are explained in the text.

| Luminosity class	[Fe/H] (dex)	N	a	b	c	R^2	σ
	(0, +0.5]	110	−0.021402(0.004368)	2.62304(0.02228)	−0.70015(0.03360)	0.993	0.043
			$T = -4.90$	$T = 117.72$	$T = -20.84$		
			$p = 0.000$	$p = 0.000$	$p = 0.000$		
Main sequence	(−0.5, 0]	102	−0.034443(0.004107)	2.58820(0.02807)	−0.66283(0.03011)	0.989	0.038
			$T = -8.39$	$T = 92.22$	$T = -22.01$		
			$p = 0.000$	$p = 0.000$	$p = 0.000$		
	(−1, −0.5]	26	−0.03266(0.01207)	2.4366(0.1004)	−0.63172(0.05707)	0.979	0.031
			$T = -2.71$	$T = 24.27$	$T = -11.07$		
			$p = 0.013$	$p = 0.000$	$p = 0.000$		
	(0, +0.5]	50	−0.002031(0.000630)	2.76866(0.03730)	−0.92365(0.05313)	0.992	0.040
			$T = -2.48$	$T = 74.22$	$T = -17.38$		
			$p = 0.014$	$p = 0.000$	$p = 0.000$		
	(−0.5, 0]	64	−0.012175(0.005475)	2.77782(0.02874)	−0.93117(0.04992)	0.996	0.036
			$T = -2.22$	$T = 96.65$	$T = -18.65$		
			$p = 0.030$	$p = 0.000$	$p = 0.000$		
Sub-giant	(−1, −0.5]	35	−0.014890(0.008362)	2.04629(0.08635)	−0.52484(0.04988)	0.959	0.029
			$T = -2.15$	$T = 23.70$	$T = -10.52$		
			$p = 0.039$	$p = 0.000$	$p = 0.000$		
	(−3, −1]	38	−0.004800(0.000810)	1.9139(0.1289)	−0.59024(0.04176)	0.926	0.030
			$T = -1.59$	$T = 14.85$	$T = -14.13$		
			$p = 0.038$	$p = 0.000$	$p = 0.000$		
	(0, +0.5]	57	0.003814(0.007765)	3.23331(0.04865)	−1.39634(0.07903)	0.989	0.034
Giant			$T = 0.49$	$T = 66.47$	$T = -17.67$		
			$p = 0.625$	$p = 0.000$	$p = 0.000$		
	(−0.5, 0]	62	−0.004697(0.006729)	3.07446(0.04036)	−1.24802(0.07181)	0.993	0.034
			$T = -0.70$	$T = 76.17$	$T = -17.38$		
			$p = 0.488$	$p = 0.000$	$p = 0.000$		

3.2. Transformation equations according to the luminosity classes and metallicities of stars

The sample stars are separated into different metallicity intervals, and transformation equations are derived for three luminosity classes of stars in each metallicity interval, as explained in the following. Main sequence and sub-giant stars occupy the metallicity intervals $0 < [Fe/H] \le +0.5$ dex, $-0.5 < [Fe/H] \le 0$ dex, $-1 < [Fe/H] \le -0.5$ dex, additionally sub-giants occupy the interval $-3 < [Fe/H] \le -1$ dex, while giants cover the metallicity intervals $0 < [Fe/H] \le 0.5$ dex and $-0.5 < [Fe/H] \le 0$ dex. We used the Equation (4) and estimated the numerical values of the coefficients *a*, *b*, and *c* for each metallicity interval and luminosity class by the procedure explained in Section 3.1. Result are tabulated in Table 5. The squared correlation coefficients in this table are higher than those in Table 4. Also, the standard deviations in Table 4 reduced by 30%. Comparison of the observed $(U - V)_0$ colour indices and the estimated ones via Equation (4) is given in Figure 9. As it can be seen easily, there is no any systematic deviations in the distribution of residuals for $(U - V)_0$ colour index. They are smaller than the those plotted in Figure 8, as well. However, we should note that the coefficient *a* estimated for the metallicity intervals of giants does not promise accurate $(U - V)_0$ colour index estimation.

4. Summary and discussion

In this study, we used 556 stars with accurate spectroscopic, photometric, and astrometric data and derived transformation equations between *GALEX* and *UBV* colours. Thus, the *U* magnitudes of the stars would be estimated more accurately by means of *FUV* and *NUV* magnitudes which are observed outside of the Earth atmosphere. Transformation equations are derived as a function of (only) the luminosity class and as a function of both the luminosity class and metallicity. In both cases, the statistical results promise accurate $U - V$ colours for the main sequence and sub-giant stars, estimated by using the *FUV* and *NUV* magnitudes. However, the same case does not hold for the giants.
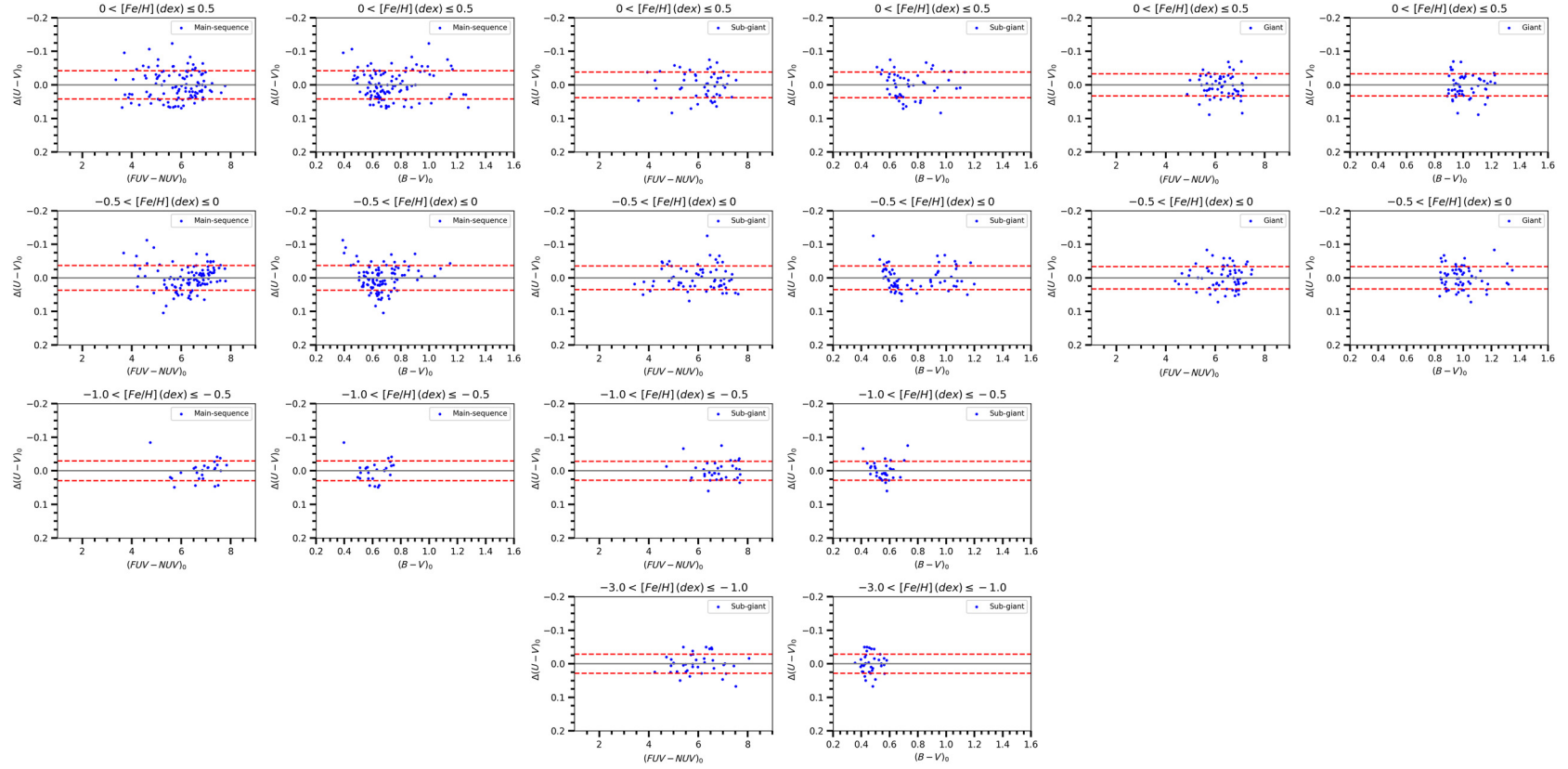
Figure 9. Colour residuals for the sample stars in terms of $(FUV − NUV)_0$ and $(B − V)_0$ colours for different luminosity classes and metallicities, as indicated in the panels. Dashed lines denote $\pm 1\sigma$ prediction levels.
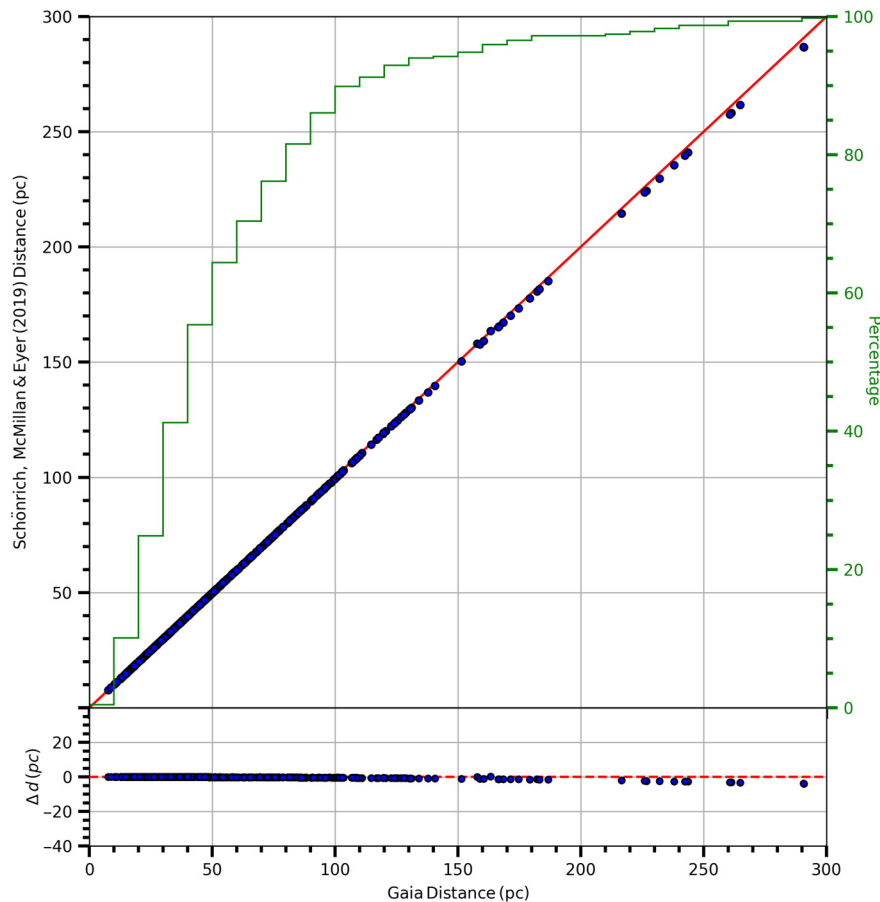
Figure 10. Comparison of the distances for the sample stars estimated via *Gaia* DR2 trigonometric parallaxes and statistical method of Schönrich et al. (2019). The distances calculated by two different methods are quite compatible with one-to-one line.

We used the inverted parallaxes as a distance estimate when calculating the interstellar absorption. However, Schönrich et al. (2019) have shown that the *Gaia* DR2 parallaxes can be biased. We compared the distances estimated via *Gaia* DR2 trigonometric parallaxes and the ones of Schönrich et al. (2019) which are obtained by a statistical method to see the impact of the distances of the stars on the analysis, as explained in the following. The mean of the differences between the distances estimated by two procedures and the corresponding standard deviation are −0.10 pc and 0.66 pc, respectively. As seen in Figure 10, almost all distances fit with the one-to-one straight line. Hence, we do not expect any systematic uncertainty for our results.
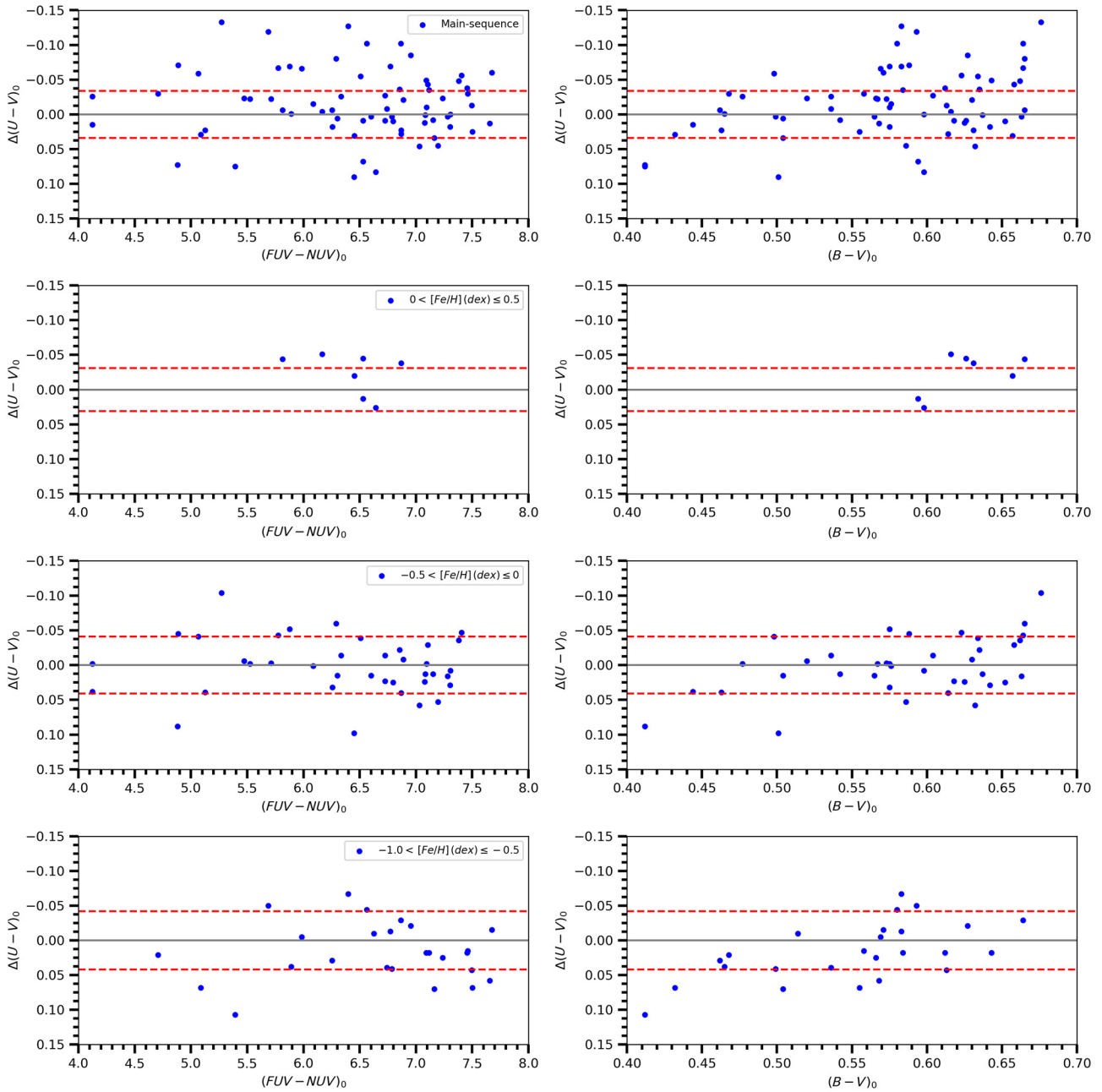
We compared the spectroscopic atmospheric model parameters taken from 14 different papers in the literature to investigate the confirmation of their homogeneity. Figures A1, A2, and A3 show that the three parameters, $T_{\rm eff}$, $\log g$, and [Fe/H] lie on the one-to-one line in the corresponding figure. Hence, we can argue that the atmospheric model parameters taken from different studies are in an agreeable homogeneity.

The transformation equations are applied to the F-G type main sequence stars Tunçel Güçtekin et al. (2016) which are provided with accurate photometric data. The sample of stars in the cited study reduced from 168 to 70 due to the absence of *FUV* and *NUV* magnitudes in *GALEX* DR7 (Bianchi et al. 2017) database. We used the corresponding coefficients in Tables 4 and 5 and

estimated the $(U - V)_0$ colours of 70 stars in question. Residuals (Figure 11) and the statistical results (Table 6) show that combination of the luminosity class and metallicity provides more accurate $(U - V)_0$ colours relative to the ones estimated by considering only the luminosity class. We should emphasize that the results corresponding only to the luminosity class are also consistent.

The transformation equations between the *GALEX* and *UBV* colours would be used for estimation of the *U* magnitude of stars for which this magnitude cannot be observed accurately. This is important for the intermediate spectral-type main sequence stars. Because the *U* magnitude thus obtained, i.e. $U_{\rm est}$, would be combined with the *B* magnitude of *UBV* photometric system and the $U_{\rm est} - B$ colour would be used in the (photometric) metallicity estimation which is important in studying the chemical structure and evolution of our Galaxy.

Figure 11. Colour residuals for 70 main sequence stars taken from Tunçel Güçtekin et al. (2016) in terms of $(FUV - NUV)_0$ (left column) and $(B - V)_0$ (right column). Residuals for stars with different metallicities are indicated in the panels. Dashed lines show $\pm 1\sigma$ prediction levels.

Table 6. Statistical results based on the comparison of the observed and calculated $(U - V)_0$ colours according to the coefficients in Tables 4 and 5 (sum of differences ($\Sigma(\Delta(U - V)_0)$), means of differences ($\Sigma(\Delta(U - V)_0)/N$), and standard deviations of differences $\sigma_{\Sigma(\Delta(U-V)_0)/N}$) for 70 main sequence stars.

[Fe/H] (dex)	N	Coefficients in Table 4			Coefficients in Table 5		
		$\Sigma(\Delta(U - V)_0)$	$\Sigma(\Delta(U - V)_0)/N$	$\sigma_{\Sigma(\Delta(U-V)_0)/N}$	$\Sigma(\Delta(U - V)_0)$	$\Sigma(\Delta(U - V)_0)/N$	$\sigma_{\Sigma(\Delta(U-V)_0)/N}$
$0 < [Fe/H] \leq 0.5$	7	0.204	0.029	0.035	−0.159	−0.023	0.031
$-0.5 < [Fe/H] \leq 0$	38	−0.501	−0.013	0.044	0.059	0.002	0.041
$-1 < [Fe/H] \leq -0.5$	25	−0.837	−0.033	0.051	0.422	0.017	0.042

References

Ak, S., Bilir, S., Karaali, S., Buser, R., & Cabrera-Lavers, A. 2007, NewA, 12, 605

Ak, S., et al. 2014, PASA, 31, 14

Bahcall, J. N., & Soneira, R. M. 1980 ApJS, 44, 73

Banks, T., Yontan, T., Bilir, S., & Canbay, R. 2020, JApA, 41, 6

Benjamin, R. A., et al. 2005, ApJ, 630L, 149

Bensby, T., Feltzing, S., & Oey, M. S. 2014, A&A, 562, A71

Bianchi, L., Shiao, B., & Thilker, D. 2017, ApJS, 230, 24

Bilir, S., Karaali, S., & Tunçel, S. 2005, AN, 326, 321

Bilir, S., Karaali, S., Ak, S., Yaz, E., Cabrera-Lavers, A., & Coşkunoğlu, K. B. 2008a, MNRAS, 390, 1569

Bilir, S., et al. 2008b, PASA, 25, 69

Bilir, S., et al. 2011, MNRAS, 417, 2230

Bilir, S., et al. 2012, PASA, 29, 121

Bilir, S., Önal, Ö., Karaali, S., Cabrera-Lavers, A., & Çakmak, H. 2013, Ap&SS, 344, 417

Boesgaard, A. M., et al. 2011, ApJ, 743, 140

Bostancı, Z. F., et al. 2018, Ap&SS, 363, 143

Brewer, J. M., Fischer, D. A., Valenti, J. A., & Piskunov, N. 2016, ApJS, 225, 32

Bressan, A., et al. 2012, MNRAS, 427, 127

Cardelli, J. A., Clayton, G. C., & Mathis, J. S. 1989, ApJ, 345, 245

Carney, B. W. 1979, AJ, 84, 515

Carrasco, G., Loyola, P., Moreno, H., & Ledoux, C. 2010, yCat, 2303

Chen, Y., Bressan, A., Girardi, L., Marigo, P., Kong, X., & Lanza, A. 2015, MNRAS, 452, 1068

Chonis, T. S., & Gaskell, C. M. 2008, AJ, 135, 264

Covey, K. R., et al. 2007, AJ, 134, 2398

Cross, N. J. G., et al. 2012, A&A, 548A, 119

Çelebi, M., Bilir, S., Ak, S., Ak, T., Bostancı, Z. F., & Yontan, T. 2019, Ap&SS, 364, 172

da Silva, R., Milone, A. D. C., & Rocha-Pinto, H. J. 2015, A&A, 580, 24

Delgado Mena, E., Tsantaki, M., Adibekyan, V. Zh., Sousa, S. G., Santos, N. C., Gonzalez Hernandez, J. I., & Israelian, G. 2017, A&A, 606A, 94

Ducati, J. R. 2002, VizieR Online Data Catalog, 2237

Dwek, E., et al. 1995, ApJ, 445, 716

Eker, Z., et al. 2018, MNRAS, 479, 5491

Gaia Collaboration, et al. 2018, A&A, 616, 22

Garcia, B., Claria, J. J., & Levato, H. 1988, Ap&SS, 143, 317

Hewett, P. C., Warren, S. J., Leggett, S. K., & Hodgkin, S. T. 1996, MNRAS, 367, 454

Ishigaki, M. N., Chiba, M., & Aoki, W. 2012, ApJ, 753, 64

Ivezic, Z., et al. 2008, ApJ, 684, 2871

Jofré, P., et al. 2015, A&A, 582A, 81

Johnson, H. L., & Morgan, W. W. 1953, MNRAS, 113, 468

Jordi, C., et al. 2006, MNRAS, 367, 290

Juric, M., et al. 2008, ApJ, 673, 864

Karaali, S., Ak, S. G., Bilir, S., Karataş, Y., & Gilmore, G. 2003a, MNRAS, 343, 1013

Karaali, S., Bilir, S., Karataş, Y., & Ak, S. G. 2003b, PASA, 20, 165

Karaali, S., Karataş, Y., Bilir, S., Ak, S. G., & Hamzaoğlu, E. 2003c, PASA, 20, 270

Karaali, S., Bilir, S., & Hamzaoğlu, E. 2004, MNRAS, 355, 307

Karaali, S., Bilir, S., & Tunçel, S. 2005, PASA, 22, 24

Karaali, S., Bilir, S., Ak, S., Yaz, E., & Coşkunoğlu, B. 2011, PASA, 28, 95

Karataş, Y., & Schuster, W. 2006, MNRAS, 371, 1793

Kim, B., et al. 2016, ApJS, 222, 19

Koen, C., Kilkenny, D., van Wyk, F., & Marang, F. 2010, MNRAS, 403, 1949

Lopez-Corredoira, M., Cabrera-Lavers, A., & Gerhard, O. E. 2005, A&A, 439, 107

Lopez-Corredoira, M., Lee, Y. W., Garzon, F., & Lim, D. 2019a, A&A, 627A, 3

Lopez-Corredoira, M., SylosLabini, F., Kalberla, P. M. W., & Allende Prieto, C. 2019b, AJ, 157, 26

Luck, R. E. 2017, AJ, 153, 21

Maldonado, J., & Villaver, E. 2016, A&A, 588, 98

Marshall, D. J., Robin, A. C., Reylé, C., Schultheis, M., & Picaud, S. 2006, A&A, 453, 635

Martin, D. C., et al. 2005, ApJ, 619L, 1

Mermilliod, J. C. 1987, A&AS, 71, 413

Mermilliod, J. C. 1997, yCat, 2168, 0

Minniti, D., et al. 2010, NewA, 15, 433

Mishenina, T. V., Pignatari, M., Korotin, S. A., Soubiran, C., Charbonnel, C., Thielemann, F. -K., Gorbaneva, T. I., & Basak, N. Y. 2013, A&A, 552A, 128

Molenda-Zakowicz, J., et al. 2013, MNRAS, 434, 1422

Murakami, H., et al. 2007, PASJ, 59, 369

Nissen, P. E., & Schuster, W. J. 2011, A&A, 530A, 15

Oja, T. 1984, A&AS, 57, 357

Rodgers, C. T., et al. 2006, AJ, 132, 989

Roman, N. G. 1955, ApJS, 2, 195

Sandage, A., & Eggen, O. J. 1959, MNRAS, 119, 278

Sandage, A. 1969, ApJ, 158, 1115

Schlafly, E. F., & Finkbeiner, D. P. 2011, ApJ, 737, 103

Schönrich, R., McMillan, P., & Eyer, L. 2019, MNRAS, 487, 3568

Schwarzschild, M., Searle, L., & Howard, R. 1955, ApJ, 122, 353

Sitnova, T., et al. 2015, ApJ, 808, 148

Snowden, S. L., et al. 1995, ApJ, 454, 643

Skrutskie, M. F., et al. 2006, AJ 131, 1163

Smith, J. A., et al. 2002, AJ, 123, 2121

Straizys, V., & Lazauskaite, R. 2009, BaltA, 18, 19

Tang, J., et al. 2014, MNRAS, 445, 428

Tunçel Güçtekin, S., Bilir, S., Karaali, S., Ak, S., Ak, T., & Bostanc, Z. F. 2016, Ap&SS, 361, 18

Tunçel Güçtekin, S., Bilir, S., Karaali, S., Plevne, O., Ak, S., Ak, T., & Bostanci, Z. F. 2017, Ap&SS, 362, 17

Tunçel Güçtekin, S., Bilir, S., Karaali, S., Plevne, O., & Ak, S. 2019, AdSpR, 63, 1360

Wallerstein, G. 1962, ApJS, 6, 407

Wright, E. L., et al. 2010, AJ, 140, 1868

Yaz, E., et al. 2010, AN, 331, 807

Yaz, E., & Karaali, S. 2010, NewA, 15, 234

Yontan, T., et al. 2019, Ap&SS, 364, 152

York, D. G., et al. 2000, AJ, 120, 1579

Yuan, H. B., Liu, X. W., & Xiang, M. S. 2013, MNRAS, 430, 2188
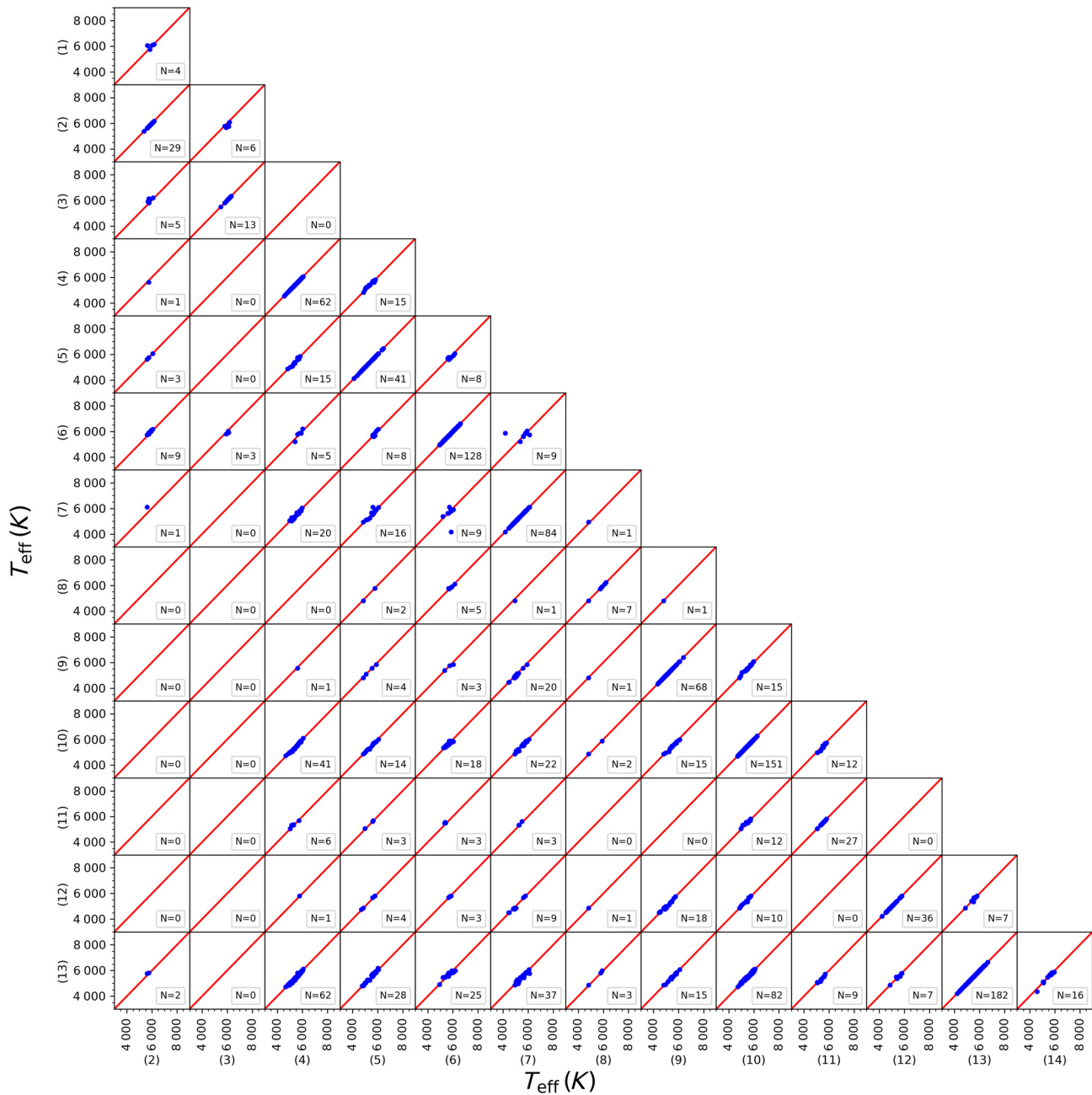
Figure A1. Corner plot showing a comparison of T_{eff} for overlapping stars in 14 research groups. The numbers indicate the research groups: Boesgaard et al. (2011), (2) Nissen & Schuster (2011), (3) Ishigaki et al. (2012), (4) Mishenina et al. (2013), (5) Molenda-Zakowicz et al. (2013), (6) Bensby et al. (2014), (7) da Silva et al. (2015), (8) Sitnova et al. (2015), (9) Jofré et al. (2015), (10) Brewer et al. (2016), (11) Kim et al. (2016), (12) Maldonado & Villaver (2016), (13) Luck (2017), (14) Delgado Mena et al. (2017).
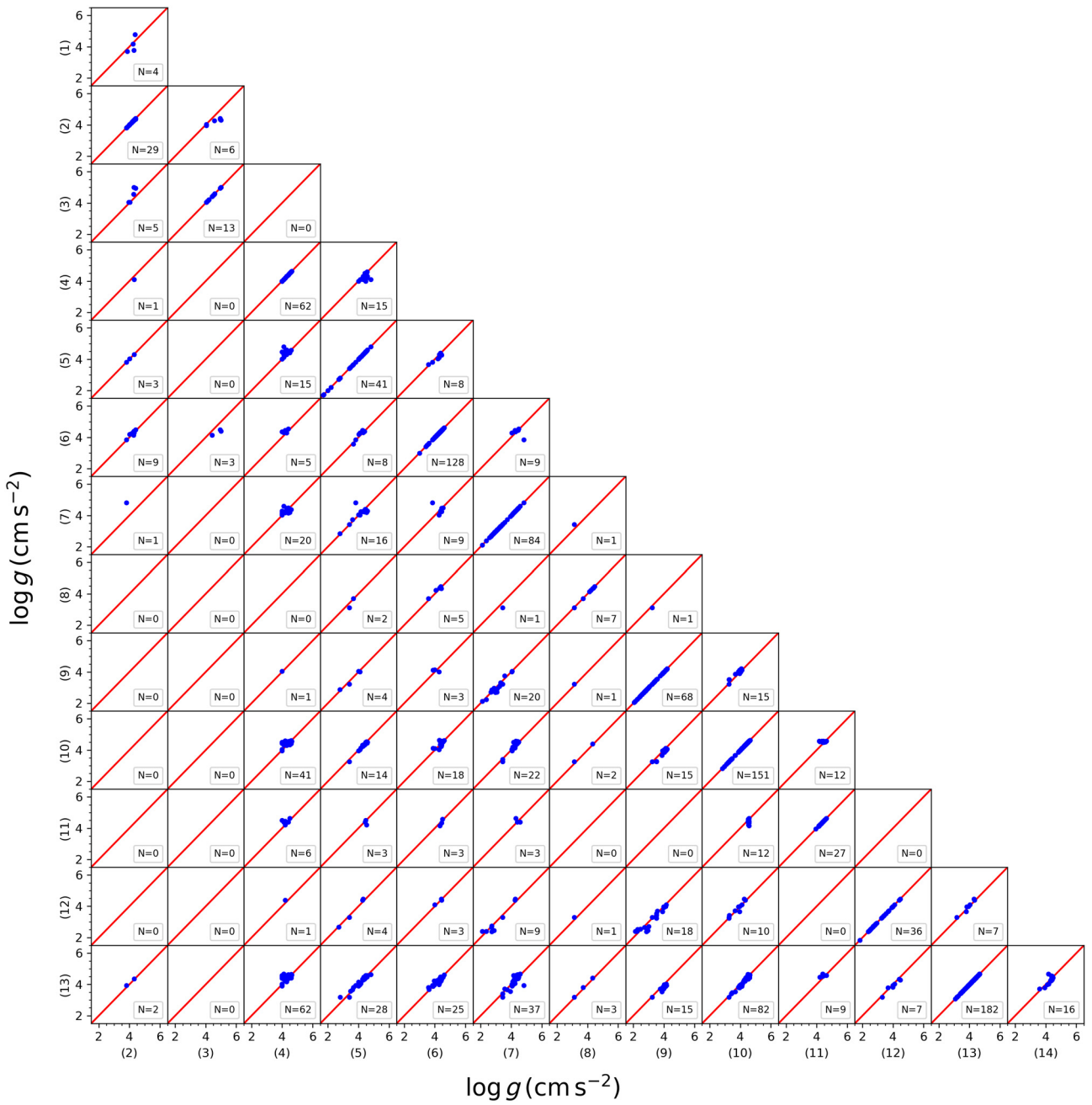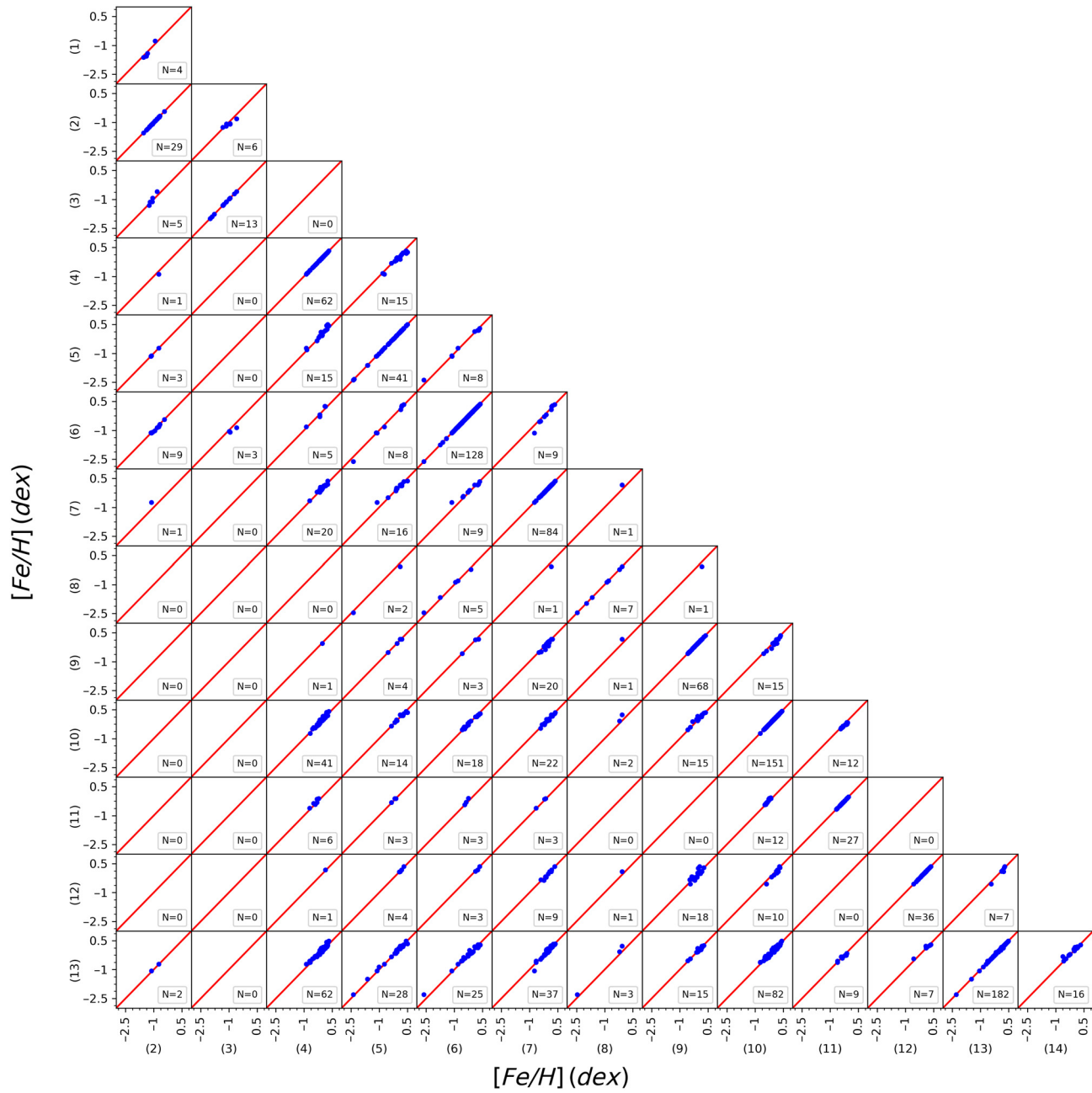
Figure A2. Corner plot showing a comparison of log *g* for overlapping stars in 14 research groups. The numbers indicate the research groups as in Figure A1.

Figure A3. Corner plot showing a comparison of [Fe/H] for overlapping stars in 14 research groups. The numbers indicate the research groups as in Figure A1.